Theory of anomalous chemical transport in random fracture networks

Brian Berkowitz and Harvey Scher
Department of Environmental Sciences and Energy Research, Weizmann Institute of Science, 76100 Rehovot, Israel
(Received 28 October 1997)

We show that dominant aspects of chemical (particle) transport in fracture networks—non-Gaussian propagation—result from subtle features of the steady flow-field distribution through the network. This is an outcome of a theory, based on a continuous time random walk formalism, structured to retain the key space-time correlations of particles as they are advected across each fracture segment. The approach is designed to treat the complex geometries of a large variety of fracture networks and multiscale interactions. Monte Carlo simulations of steady flow in these networks are used to determine the distribution of velocities in individual fractures as a function of their orientation. The geometry and velocity distributions are used, in conjunction with particle mixing rules, to map the particle movement between fracture intersections onto a joint probability density $\psi(\mathbf{r},t)$. The chemical concentration plume and breakthrough curves can then be calculated analytically. Particle tracking simulations on these networks exhibit the same non-Gaussian profiles, demonstrating quantitative agreement with the theory. The analytic plume shapes display the same basic behavior as extensive field observations at the Columbus Air Force Base, Mississippi. The quantitative correlation between the time dependence of the mean and standard deviation of the field plumes, and their shape, is predicted by the theory. [S1063-651X(98)15805-1]

PACS number(s): 47.55.Mh, 91.60.−x, 92.40.−t

I. INTRODUCTION

Chemical transport in geological formations is often observed to be anomalous, i.e., non-Gaussian. The advance of a chemical or tracer plume is anomalous if the transport coefficients are either space or time scale dependent. Such transport has been observed frequently in field studies, where dispersion of contaminants is studied by pulse injection of a tracer into the flow field of a saturated heterogeneous or fractured formation. In a large-scale field study carried out in a heterogeneous alluvial aquifer at the Columbus Air Force Base (Mississippi), for example, bromide was injected as a pulse and traced over a 20 month period by sampling from an extensive three-dimensional well network [1,2]. The tracer plume that evolved was remarkably asymmetric (Fig. 1), and cannot be described by classical Gaussian models. Tracer injection studies in well-mapped fractured formations, such as at the Stripa site (Sweden), also display a variety of anomalous, clearly non-Gaussian, types of behavior (e.g., Ref. [3]).

These extensive and costly field studies are carried out because the understanding and quantification of flow and contaminant transport in fractured and heterogeneous formations is of considerable practical importance in terms of exploitation and preservation of aquifers. Particular emphasis has been placed on evaluating properties of hard rock formations as potential underground repository sites for the storage of radioactive and industrial wastes [4]. As a consequence, major efforts have been devoted over the last few years to the development of realistic theoretical models capable of simulating flow and transport processes in fractured and heterogeneous porous formations. These efforts have led to significant understanding of the dynamics of flow and transport processes in these disordered systems.

Predictive capabilities related to real fractured and heterogeneous media remain, however, severely limited [5]. In part, this is due to the very complex nature of fracture networks in the subsurface, which precludes complete and detailed mapping of fractures. As a result, studies must rely on extrapolation of exposed features to generate a statistical characterization of fracture systems. This analysis is demanding, as fractures exist in a broad range of geological formations and rock types, and are produced under a variety of geological and environmental processes. As a result of the variability in rock properties and structures, as well as the variety of fracturing mechanisms, fracture sizes range from microfissures of the order of microns to major faults of the order of kilometers, while fracture network patterns range from relatively regular polygonal arrangements to apparently random distributions. The hydraulic and transport properties of these formations vary considerably, being largely dependent on the degree of fracture interconnection, aperture variations in the fractures, and chemical characteristics of the fractures and host rock.

A number of recent studies have addressed theoretical aspects of anomalous transport, using a variety of stochastic treatments (e.g., [6–11]). The spatial dependence of transport coefficients is usually explained as being due to permeability fields with coherence lengths varying over many scales. However, spatial variability is not in itself sufficient to explain all anomalies in plume shapes. For example, the hydraulic conductivity field at the Columbus site [2] is relatively well distributed (see Fig. 2 of [2]), and the approximate diagnostic transport models used to study the plume evolution capture only some of the key characteristics. Modeling attempts to quantify tracer transport at the Stripa site (e.g., Ref. [3]) have also met with limited ability to predict the full evolution of the plume.

The principal purpose of this paper is to demonstrate persistent time-dependent anomalies in a model fracture system—a well-connected network with elements of randomly varying lengths, apertures, and orientations—in which

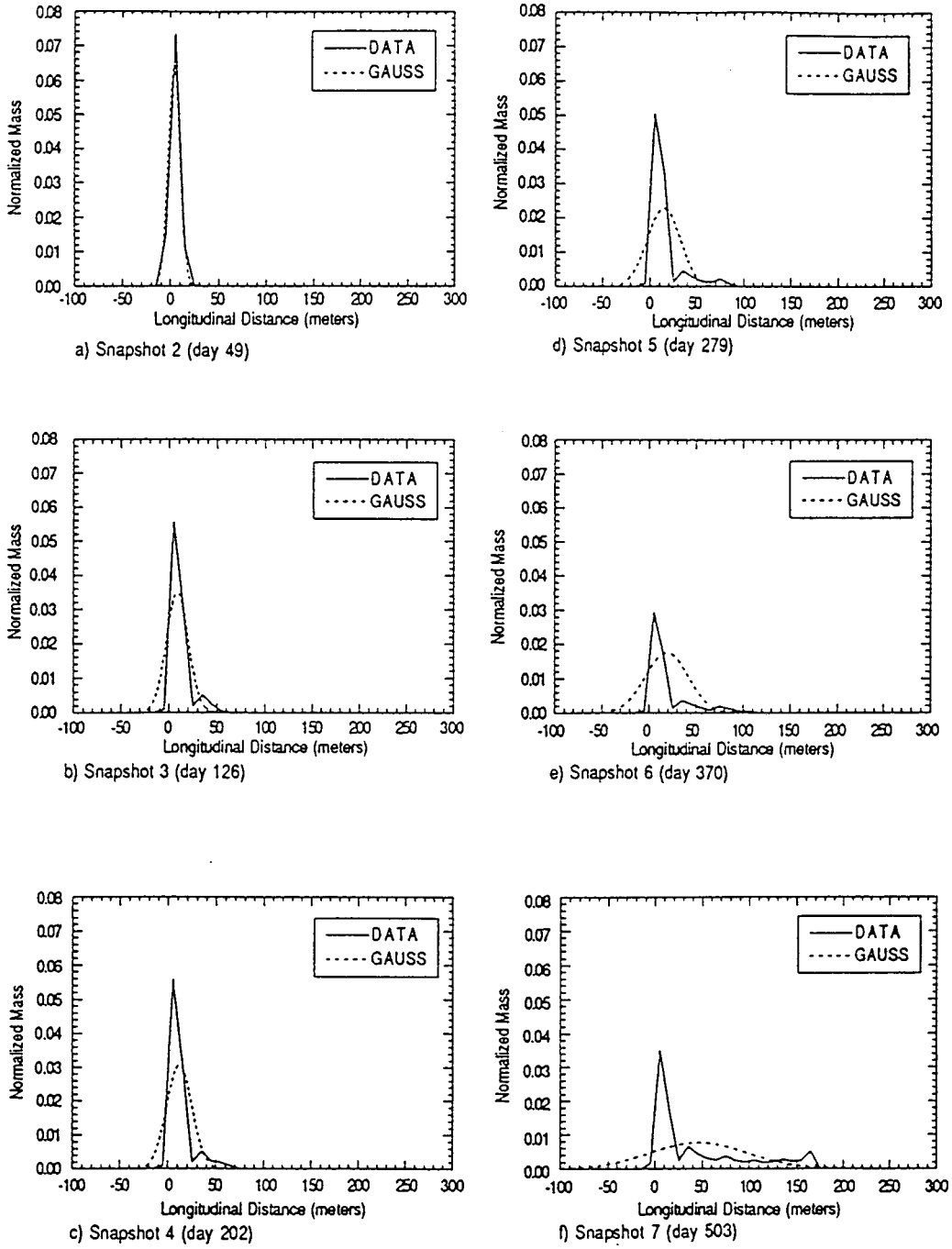

FIG. 1. Longitudinal distribution of an injected tracer in a heterogeneous aquifer, at six points in time. The dashed line represents mass distribution for tracer migrating according to the classical Gaussian model (after Ref. [2], Fig. 7).

the spatial scale of observation is much greater than the element sizes. We show that anomalous time-dependent transport depends on subtle features of the random velocity distribution $\Phi(\mathbf{v})$, determined from steady-state flow through even simple ''homogeneously heterogeneous'' systems (cf. Ref. [12] for a short, preliminary version of this work). We then extend our analysis to field data from experiments carried out in a heterogeneous geological formation (aquifer), and find strong evidence of time-dependent anomalous transport.

In this initial application there is a strong interplay between the analytic formalism and extensive simulations of steady flow in numerical discrete fracture models (such as shown in Fig. 2; see below). The geometry and the velocity distribution are used, in conjunction with particle mixing rules, to map the particle movement between fracture intersections onto a joint probability density $\psi(\mathbf{s},t)$, the probability per time for a transition between fracture intersections separated by $\mathbf{s}$ with a difference of arrival times of t. In this mapping we retain the key space-time correlations of particles as they are advected across each segment and dispersed by the random velocity field of the network. This approach makes tractable the determination of the full evolution of the chemical density (plume), $P(\mathbf{s},t)$, in large systems, in both two and three dimensions. $P(\mathbf{s},t)$ is compared with many realizations of particle tracking simulations (PTS's) on the

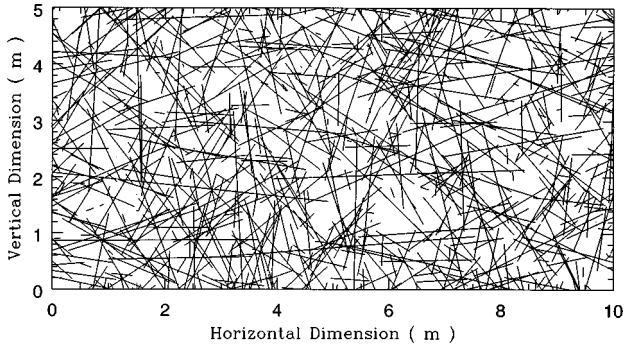

FIG. 2. A portion of a typical two-dimensional fracture network used in the numerical simulations.

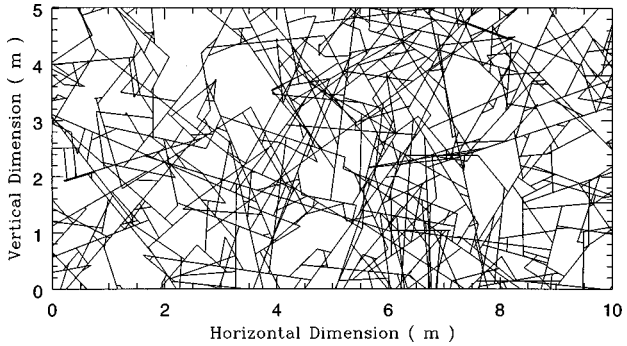

FIG. 3. A portion of a typical ''backbone'' of a two-dimensional fracture network.

same networks used to obtain $\Phi(\mathbf{v})$. We also show that the key features of $P(\mathbf{s},t)$ are manifest in the field observations at the Columbus Air Force Base [1,2].

The theoretical framework that enables us to advance from $\psi(\mathbf{s},t)$ to $P(\mathbf{s},t)$ is based on a continuous time random walk (CTRW) formalism [13]. The CTRW is capable of quantifying and predicting anomalous transport. This approach allows us to account accurately for the subtle, yet critically important, features of time-dependent chemical transport that are usually neglected.

In Sec. II, we examine chemical transport in a model that simulates steady flow and transport in two-dimensional random fracture networks, and use particle tracking to demonstrate an anomalous, time-scale-dependent, dispersion. In Sec. III, we outline the formalism of our theoretical CTRW approach, and present the transport equation that we solve for chemical migration. In Sec. IV, we analyze the fracture network model, used in Sec. II, to obtain the fracture segment and segment velocity distributions. These distributions are fit with functional forms. We use these functional forms in Sec. V to calculate $\psi(\mathbf{s},t)$, and then determine the integral transforms used in the solution of the transport equation. We then analyze the evolution of the chemical plume, $P(\mathbf{s},t)$. In Sec. VI, we compare our analytical results with the ensemble averaged particle tracking simulations on the same two-dimensional random fracture networks. We also relate our analytical results to the field data of Refs. [1] and [2], mentioned above.

II. SIMULATION OF CHEMICAL TRANSPORT IN A TWO-DIMENSIONAL FRACTURE NETWORK

A. Numerical fracture network model

The numerical fracture model employed in this study [14] generates discrete fracture networks in two-dimensional rectangular regions, and solves for flow and chemical transport within these networks. The fracture networks are composed of linear, constant aperture fractures, embedded in an impermeable matrix. Fracture network realizations are generated from prescribed distributions of fracture locations, orientations, lengths, and apertures, which are assumed to be statistically independent. Fractures are generated in a region larger than the model domain, and those at the domain boundary are then truncated. This ensures that there is little decrease in fracture density near the domain boundaries. Additional details describing the method of creating the stochastic fracture networks were given in Ref. [14].

In this initial study, and following typical distributions and parameter values found in the literature (e.g., Refs. [14, 15]), numerous realizations of fracture networks were generated according to (i) uniformly distributed fracture midpoints selected randomly over the entire fracture generation region; (ii) two random fracture sets, with orientations (relative to the horizontal hydraulic head gradient) sampled from Gaussian distributions with means and standard deviations of $0.0° \pm 90°$ and $90.0° \pm 90°$; (iii) a negative exponential length distribution, with a mean length of 1.1 m, in a domain of size 18 m (x direction) $\times$ 20 m (y direction); (iv) a log-normal aperture distribution, with mean aperture of 2×10^{-5} m and a standard deviation of $\log_{10}$ aperture of 0.2 (roughly equivalent to an aperture variation of one order of magnitude); (v) a scan-line density of 7.0 fractures per meter; and (vi) a regional applied hydraulic head gradient of 0.02. Figure 2 shows a portion of a representative fracture network generated with these parameters; it is typical of the ''reasonably well-connected networks'' used frequently in theoretical studies of fracture networks (e.g., Refs. [15,16]).

In order to solve for flow and chemical transport, the fracture network is discretized into the segments between fracture intersections, with constant flow in each segment. Defining the overall flow field from left to right across the domain, all fractures and ''dangling'' segments not comprising part of the hydraulically conducting portion (or ''backbone'') of the network are removed from the domain (see Fig. 3). Specifying equations for conservation of mass at the intersections, together with suitable domain boundary conditions, results in a set of linear equations whose solution yields the distribution of pressures at the intersections. Constant hydraulic heads are prescribed around the entire domain boundary; an applied regional head gradient is specified between the two vertical boundaries, and constant head values along the two horizontal boundaries are prescribed assuming a linear change in head between the inlet and outlet (vertical) boundaries. These boundary conditions assume that the region surrounding the model domain is homogeneous, and that flow within the domain does not influence flow in the surrounding region.

Chemical transport is modeled by use of a standard particle tracking routine. Particles move in discrete steps between fracture intersections, and the time to move is calculated from the fluid velocity within the fracture segment.

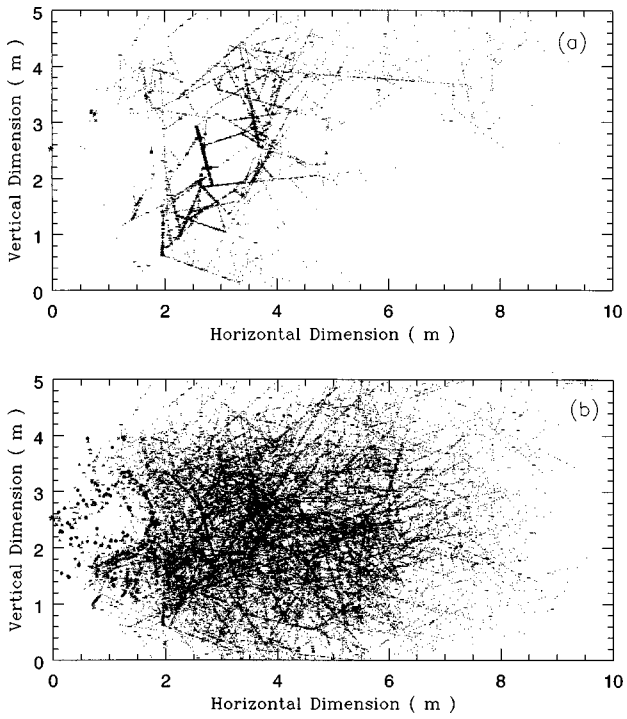

FIG. 4. Typical distributions of the chemical plume. The overall flow direction is from left to right. Particles are injected on the left vertical boundary, at the point marked by a star. The size of points is proportional to the number of particles in each cell. (a) Single fracture network realization. (b) Composite of 100 000 particles in 20 fracture network realizations.

Plug flow is assumed within each fracture, and important effects of diffusion and mechanical dispersion are manifested in the complete mixing of particles at fracture intersections, i.e., particles leaving an intersection are distributed randomly among outflowing fracture segments in proportion to their volume flow. Stream tube routing could also be implemented in the PTS's but is not considered at this stage [17]. For each fracture network realization the statistics of a number of important properties are collected and examined, as discussed in the following sections.

B. Analysis of particle tracking simulations

We consider the overall evolution of a chemical plume as it migrates through the domain. For each fracture network realization, 5000 particles are injected into the network. We illustrate important details of the nature of the chemical transport in Fig. 4. To minimize boundary effects and the loss of particles from the system (as seen in Fig. 4), we must increase the domain size in both directions with increasing plume evolution time. Thus the computationally feasible size of the domain limits the times at which the plume distribution can be simulated. In the simulation results analyzed here, particles enter the system at fracture intersections lying within a small window centered at $x=2$ and $y=10$, in an 18×20-m^2 domain. Note that with the exception of the illustrations shown in Figs. 2, 3, and 4, all simulations in this study used the 18×20-m^2 domain.

Two principal features of the chemical transport pattern can be observed in Fig. 4. First, the transport pattern is anomalous, in that very significant quantities of particles

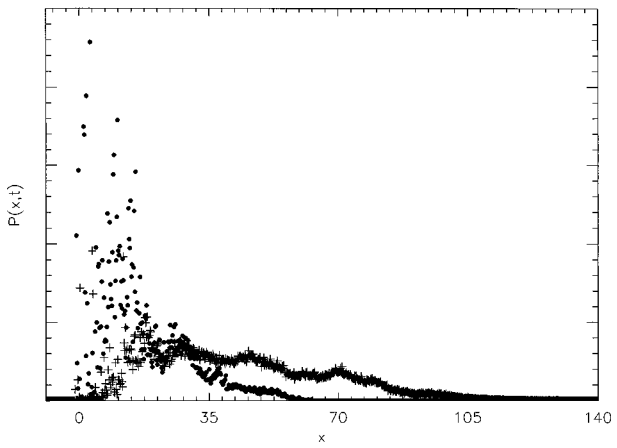

FIG. 5. The vertical average (along the y axis) of $P(\mathbf{s},t)$, defined as $P(x,t)$ (in arbitrary units) vs x (units of length are s_o and time $s_o/2v_o$, where all particle injection points are translated to $x=0$). Simulation results averaged over 50 realizations for $t=20$ (●) and 50 (+).

(chemical mass) remain near the point of injection on time scales where the ''average'' mean position continually advances across the domain. Second, while these particles are held back, a finite percent of particles advances quickly across the system, well ahead of the mean. An obvious explanation is that these particles experience a higher frequency of high velocity fracture segments, along their paths, permitting the faster chemical transport. Recognition of these two features, and their interplay, which arise (possibly somewhat surprisingly) even in a relatively simple system, forms the basis for the use of the CTRW theory which we develop below.

We can further illustrate these two key features by averaging the number of particles, along the vertical (y) direction. Figure 5 presents the vertical (normalized) average of $P(\mathbf{s},t)$, defined as $P(x,t)$ (in arbitrary units) vs x (units of length are s_o, an average distance between intersections and time $s_o/2v_o$, where v_o is a characteristic velocity of the flow distribution; s_o and v_o will be defined more precisely below). The progression of the normalized plume, $P(x,t)$, is highly non-Gaussian. The peak of the distribution remains close to the injection point, while a finite fraction of relatively fast particles continually stretches out the concentration profile. It is interesting to note that anomalous transport of this nature is well established in the electronic transport literature [18]. Shapes very similar to those shown in Fig. 5 have been measured directly in amorphous chalcogenides for propagating packets of electric charge [19].

The anomalous nature of the evolving migration pattern can be demonstrated more quantitatively by calculating the mean $\overline{l}(t)$ and standard deviation $\overline{\sigma}(t)$ of the chemical plume distribution over time, $P(x,t)$. In Gaussian transport, which is an outcome of the central limit theorem, we have $\overline{l}(t)\propto t$ and $\overline{\sigma}(t)\propto t^{0.5}$, and the position of the peak of the distribution coinciding with $\overline{l}(t)$. As we will discuss in Sec. V and VI, we find time exponents for our particle tracking simulations that are significantly different. The importance of these exponents is best discussed in the context of the theory which we now develop to account for this phenomenon.

III. CONTINUOUS TIME RANDOM WALKS

A random walk (RW) describes the consequences of the accumulation of many random transitions between states, e.g., points in a Euclidean space or a multidimensional phase space. The transitions are generated by choosing from a specific distribution; simplicity is assured if the state of the walker is determined only by transition from its previous state (e.g., there are no persistent correlations between transitions). The choice of distribution will be our major challenge in the application described in the present study of fracture networks.

The accumulation aspect of a RW will be illustrated by a simple example: the walker makes transitions between points on a lattice at regular time intervals. Then if $P_n(l)$ is the probability that the walker is at point l after n steps (transitions),

$$P_{n+1}(l)=\sum_{l'} p(l,l')P_n(l'), \tag{1}$$

where $p(l,l')$ is the transition probability for a jump from l' to l with

$$\sum_{l'} p(l,l')=1. \tag{2}$$

The key structure is the recursive relation in Eq. (1), and hence the accumulation of many transitions.

The starting point of our RW application is a generalization of this example from discrete time n to continuous time (CTRW) with the spatial state description remaining discrete,

$$R(\mathbf{s},t)=\sum_{s'} \int_0^t \psi(\mathbf{s}-\mathbf{s}',t-\tau)R(\mathbf{s}',\tau)d\tau, \tag{3}$$

where $R(\mathbf{s},t)$ is the probability per time for a particle to just arrive at a site $\mathbf{s}$ at time t, and $\psi(\mathbf{s},t)$ is the probability per time for a transition between sites separated by $\mathbf{s}$ with a difference of arrival times of t [13]. The sites are on a lattice, and we assume periodic boundary conditions, i.e., $\mathbf{s}=\Sigma_i s_i\mathbf{a}_i$, $|\mathbf{a}_i|=a$, the lattice constant, with $\{s_i\}$ integers and $s_i+j_iN\rightarrow s_i$, for arbitrary integer j's, where Na is the length of the lattice, $s_i=-(N-1)/2,\ldots,(N-1)/2$. Continuous time introduces a subtlety which need not be considered in the example in Eq. (1). We have to distinguish now between the walker just arriving at the site and the probability of remaining at the site for a random time before the next jump. We define the analogy to P_n by

$$P(\mathbf{s},t)=\int_0^t \Pi(t-\tau)R(\mathbf{s},\tau)d\tau, \tag{4}$$

where

$$\Pi(t)=1-\int_0^t \psi(\tau)d\tau \tag{5}$$

is the probability to remain on a site and

$$\psi(\tau)=\sum_s \psi(\mathbf{s},\tau). \tag{6}$$

It is important to note that advective and dispersive transport mechanisms are not separate terms in Eq. (3), but are, rather, inextricably combined.

The form of Eq. (3) is that of a convolution in space and time which can be solved by discrete Fourier transform ($\mathcal{F}$) and Laplace transform ($\mathcal{L}$), respectively,

$$\mathcal{R}(\mathbf{k},u)=1/[1-\Lambda(\mathbf{k},u)] \tag{7}$$

$k_i=-(2\pi/N)[(N-1)/2],\ldots,(2\pi/N)[(N-1)/2]$, with $\mathcal{R}$ the discrete Fourier transform and Laplace transform of $R(\mathbf{s},t)$, and similarly for $\psi(\mathbf{s},t)$

$$\Lambda(\mathbf{k},u)\equiv\mathcal{F}\{\psi^*(\mathbf{s},u)\}=\sum_s \exp(-i\mathbf{k}\cdot\mathbf{s})\psi^*(\mathbf{s},u) \tag{8}$$

$$\psi^*(\mathbf{s},u)\equiv\mathcal{L}\{\psi(\mathbf{s},t)\}=\int_0^\infty \exp(-ut)\psi(\mathbf{s},t)dt \tag{9}$$

The total transition rate must be normalized, hence

$$\Lambda(0,0)=1. \tag{10}$$

Also, from Eqs. (6) and (8),

$$\Lambda(0,u)=\psi^*(u) \tag{11}$$

which is the $\mathcal{L}$ of $\psi(\tau)$. Finally, the principal object of our calculation is given by

$$P(\mathbf{s},t)=N^{-d}\sum_k \exp(i\mathbf{k}\cdot\mathbf{s})\gamma(\mathbf{k},t), \tag{12}$$

where

$$\gamma(\mathbf{k},t)=\mathcal{L}^{-1}\{\mathcal{R}(\mathbf{k},u)[1-\psi^*(u)]/u\},$$

using the $\mathcal{L}$ of Eqs. (4) and (5) and $\mathcal{L}^{-1}$ is the inverse $\mathcal{L}$. The function $P(\mathbf{s},t)$ describes the evolution of the chemical plume and, in principle, can be determined analytically for an arbitrary $\psi(\mathbf{s},t)$. In practice, this can be quite difficult, as it involves an inverse Laplace transform $\mathcal{L}^{-1}$. We will describe a general method to accomplish the inversion which will be considered in detail in Sec. 5.

We conclude this section on the formal structure of the CTRW with the definition of the first passage time distribution $F(\mathbf{s},t)$, which implicitly is

$$R(\mathbf{s},t)=\delta_{\mathbf{s},0}\delta(t-0^+)+\int_0^t F(\mathbf{s},\tau)R(0,t-\tau)d\tau, \tag{13}$$

with $\delta_{i,j}$ being the Kronecker delta function and $\delta(t-t_o)$, the Dirac delta function, or, in Laplace space,

$$F^*(\mathbf{s},u)=[R^*(\mathbf{s},u)-\delta_{\mathbf{s},0}]/R^*(0,u), \tag{14}$$

As evinced in Eq. (13), the first passage time distribution $F(\mathbf{s},t)$ appears in another integral equation for R with a straightforward meaning. We recall $R(\mathbf{s},t)$ is the probability per time that the walker just arrives at $\mathbf{s}$ at time t but not

necessarily for the first time. The walker might have visited **s** at an earlier time τ for the first time and returned, an arbitrary number of times, in the remaining $t-\tau$, described by $R(0, t-\tau)$.

The first passage time distribution $F(\mathbf{s},t)$ is evaluated for the breakthrough curve for chemical transport, where **s** is the distance from the source to the collection plane. We note, parenthetically, that the frequent practice of measuring breakthrough curves in the laboratory by collecting samples at the outlet end of a porous medium column, and comparing these curves with a probability function, $P(x,t)$ (e.g., a solution of the classical advection-dispersion equation), is in fact an approximation. The measured breakthrough curves should be compared with the first passage time distribution, to account correctly for the ''absorbing boundary'' at the outlet, i.e., the inability of particles to diffuse in the upstream direction once they reach the column outlet.

IV. ANALYSIS AND CHARACTERIZATION OF KEY STRUCTURE AND FLOW

While numerous studies have used fracture network models such as that described in Sec. II to examine flow and contaminant transport in fracture networks, emphasis has been placed largely on characterizing effective hydraulic conductivity and contaminant dispersion patterns, mostly under steady-state conditions. However, these previous analyses have not characterized certain key controlling factors which we have clarified in defining a suitable $\psi(\mathbf{s},t)$, the probability per time for a transition between sites separated by **s** and arrival times t. Hence we focused on collecting statistics on fracture segment lengths, velocity, volumetric flow rate, fracture angle distributions for fluid leaving and entering fracture intersections, aperture distributions, and joint statistics (correlations) on pairs of these parameters. After careful examination of possible subtle correlations, we identified the key controlling factors to be the segment length distribution and the distribution of fluid velocity as a function of fracture orientation (angle) with respect to the hydraulic head gradient.

For randomly generated networks such as considered here, an exponential segment length distribution is to be expected. However, this can be distorted by including in the histogram of segment lengths ever smaller differences in the numerical position of the nodes. Thus, to define the distribution to be physically realistic and practical (since we only distinguish different pressures at nodes beyond a certain small separation), the distribution should vanish as $s\rightarrow 0$. The distribution which we fit to the data is

$$p(s)\propto s^{1/2}\exp(-s/s_o). \tag{15}$$

Based on a set of 20 fracture network realizations, for example, we find the fracture segment length distribution to follow Eq. (15), as illustrated in Fig. 6. The parameter s_o is chosen to give the best exponential fit to the data and also the peak [of Eq. (15)] close to the physically motivated cutoff at the very small segment lengths. The length scale is set by s_o, and is used in Fig. 5 to define the nondimensional length x.

The most critical characterization is the flow field. We define a distribution of fluid velocities (leaving fracture intersections), $\Phi(\mathbf{v})$, as a function of the fracture angle relative

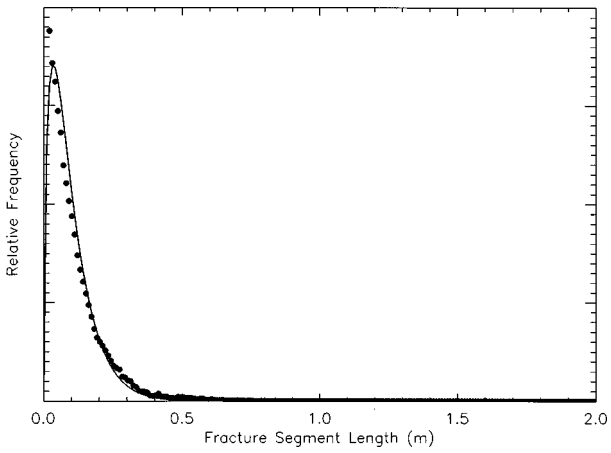

FIG. 6. Cumulative plot of the fracture segment length distribution for 20 network realizations, and the fit with Eq. (15).

to the hydraulic head gradient (Fig. 7). There are two particular features of this distribution. First, as in the case of the fracture segment length distribution, the fluid velocity frequency must tend to zero, at all angles (except for a vanishingly small range about $\pm 90°$), as the velocity approaches zero. Second, the velocity distribution, which is similar in shape to that of the segment lengths (Fig. 6), varies significantly as a function of the fracture angle: the distribution falls off exponentially at large v, $\exp[-v/v_o(\theta)]$, with a coefficient v_o that is strongly θ dependent, while the dropoff at small v is ''soft'' (algebraic). Orthogonal to the direction of the head gradient, the velocity distribution is skewed sharply

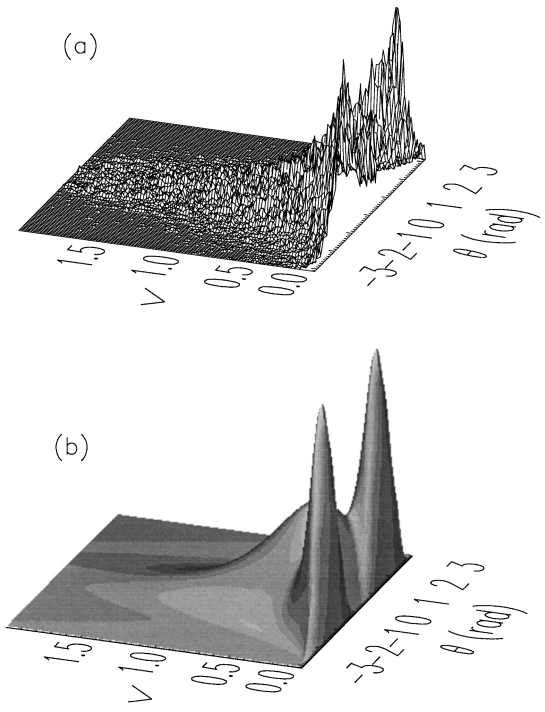

FIG. 7. The velocity distribution within fracture segments $\Phi(\mathbf{v})$. (a) A compilation of data from 20 fracture network generations. $\Phi(\mathbf{v})$ is plotted in arbitrary units as a function of v and θ, the direction of **v** with respect to the pressure gradient, (negative) along the x axis (cf. Fig. 2). The blank space on the right is the intersection with the $v=0$ plane. (b) The fit with Eq. (16).

toward the small velocity values. Figure 7(a) is a compilation of data from 20 fracture network realizations.

We have been able to obtain a very good fit to characterize this behavior by using

$$\Phi(\mathbf{v}) \propto v^{1+\beta}\left[\exp\left(-v/v_o \cos^2\frac{\theta}{2}\right) + w\ \exp(-v/v' \sin^2\theta)\right], \tag{16}$$

where β, w, v_o, and v' are parameters of the fit. The first term of the function captures the overall surface of the distribution, and the second term accounts for the two data ''spikes'' at angles roughly orthogonal to the direction of the head gradient. Figure 7(b) presents an example fit of Eq. (16) to the simulation data.

We note that essentially no correlation was found between fluid velocity and segment length, except that most of the unusually high velocity values were found to occur in small segment lengths. From our analyses, we also found little or no correlation between, for example, velocity and aperture, or velocity and volumetric flow rate other than an overall dependence of the velocity distribution on the aperture distribution. At each intersection there is no correlation between the branch velocities. Note that one can test for further correlations that extend beyond each fracture intersection (especially the higher flow rates in the forward direction) by generalizing Eq. (15) to

$$p(s|\mathbf{v}) \propto s^{1/2}[(1-\epsilon(\theta))\exp(-s/s_o) + \epsilon(\theta)\exp(-s/\xi)], \tag{17}$$

where $\epsilon(\theta)$ is a function of θ, peaked in the forward direction, and represents the small fraction of events [i.e., $\epsilon(\theta) \ll 1$] where the particle travels farther than the average distance between intersections, $\xi > s_o$.

V. CHEMICAL PLUME EVOLUTION USING CTRW

We now combine the CTRW formulation (Sec. III) and the functional distributions obtained from the simulation data (Sec. IV). We envision all the fracture intersections with a branch velocity $\mathbf{v}$. At each such site we can evaluate the fraction $f(v)$ of the particles entering the branch using the simple mixing rule discussed above, and we can subsequently determine the displacement from the site $p(s|\mathbf{v})$. We multiply the product of these two terms by the probability to encounter the velocity $\mathbf{v}$. Hence

$$\psi(\mathbf{s},t) = C_n \Phi(\mathbf{v}) p(s|\mathbf{v}) f(v), \tag{18}$$

where C_n is a normalization constant, $t = s/v$, $p(s|\mathbf{v})$ is given in Eq. (17), and $\Phi(\mathbf{v})$ is given in Eq. (16). We first consider the contribution of $f(v)$. The mixing rule is determined by the relative volume flow Q; for each v there is a distribution of apertures A, hence each choice of v corresponds to a range of $Q(=Av)$. For a large enough range one can assume that $f(v)$ is a slowly varying function of v, except for very low v, where it can be incorporated into the $\Phi(\mathbf{v})$, i.e., an effective β. For simplicity we choose $p(s|\mathbf{v})$ to be equal to the fragment distribution (15) [i.e., Eq. (17) with $\epsilon(\theta) = 0$]. The evaluation of $\epsilon(\theta)$ will be considered in future work.

The long time behavior of $\psi(\mathbf{s},t)$ in Eq. (18) is determined by the power of v in $\Phi(\mathbf{v})$ in Eq. (16), $\psi(\mathbf{s},t) \rightarrow t^{-1-\beta}$, $t \rightarrow \infty$. The asymptotic form at large time of $\psi(\mathbf{s},t)$ determines the time dependence of the mean position $\overline{l}(t)$ and standard deviation $\overline{\sigma}(t)$ of $P(s,t)$ [20,21]. In the presence of a bias (e.g., pressure gradient), and, for $0 < \beta < 1$,

$$\overline{l}(t) \propto t^{\beta}, \tag{19}$$

$$\overline{\sigma}(t) \propto t^{\beta}. \tag{20}$$

The unusual time dependence of $\overline{l}(t)$ and $\overline{\sigma}(t)$ is the hallmark of the highly non-Gaussian propagation of $P(\mathbf{s},t)$; it is a manifestation of the infinite mean (first moment) $\langle t \rangle$ of $\psi(\mathbf{s},t)$, i.e., $\psi(\mathbf{s},t)$ does not fulfill the conditions of the central limit theorem. As discussed above, this so-called anomalous dispersion has been very well documented in a large literature of electronic transport measurements in low mobility disordered semiconductors and organic films [18].

The careful determination of β, therefore, is an important and subtle feature of the random velocity distribution in a fracture network that has been largely overlooked. It is challenging to obtain a very narrow range of β values with our simulation data (recall Fig. 7). However, $\beta \sim 0.7$ was determined to fit the data well, and in Sec. VI we will show that it gives an excellent quantitative account of the $\overline{l}(t)$ and $\overline{\sigma}(t)$ of the PTS's. These results, using Eqs. (19) and (20), will be our main quantitative agreement for the PTS's.

As a first step in the explicit calculation of the analytic expression for the chemical concentration, we evaluate the Laplace transform $\psi^*(\mathbf{s},u)$ of Eq. (18). We will evaluate $\psi^*(\mathbf{s},u)$ by using the first term of Eq. (16) for $\Phi(\mathbf{v})$. The effect of the other term was found to be small. Then

$$\psi^*(\mathbf{s},u) = C_n 2 v_o^{\beta/2} s^{1/2} e^{-s/s_o} s\ \cos^{\beta}\frac{\theta}{2}\,(\sqrt{su})^{\beta} \times K_{\beta}\left(2\sqrt{su}/v_o^{1/2}\cos\frac{\theta}{2}\right) \tag{21}$$

(Ref. [22], p. 22, No. 3.2.8), where $K_{\beta}(x)$ is the modified Bessel function of order β (Ref. [23], p. 374). The Fourier transform of Eq. (21) cannot be carried out analytically. We can, however, compute the chemical concentration $P(\mathbf{s},t)$ numerically with the procedure outlined below. For our present purposes we can simplify this computation, and make the procedure more illustrative by setting $\beta = \frac{1}{2}$. We have already discussed the main quantitative predictions, Eqs. (19) and (20), for the PTS's and the criteria for highly non-Gaussian concentration transients. The main demonstration for our calculation now of the complete $P(\mathbf{s},t)$ is to exhibit the non-Gaussian behavior and a qualitative agreement with the PTS's. This can be accomplished with $\beta = \frac{1}{2}$; this results in Eq. (21) simplifying to the form

$$\psi^*(\mathbf{s},u)=C_n\sqrt{\pi v_o}s^{1/2}e^{-s/s_o}\cos\frac{\theta}{2}\,s \times\exp\left(-2s^{1/2}u^{1/2}/v_o^{1/2}\cos\frac{\theta}{2}\right), \quad -\pi\leqslant\theta\leqslant\pi. \quad (22)$$

(Ref. [22], p. 22, No. 3.2.7).

It is convenient to use a nondimensional form for u, $s_o u/2v_o\rightarrow u$ with a corresponding nondimensional form for t, $2v_o t/s_o\rightarrow t$. In computing the Fourier transform Eq. (8) of $\psi^*(\mathbf{s},u)$ in Eq. (22), we replace the lattice sum by an integral which is the value in the limit $N\rightarrow\infty$,

$$\Lambda(\boldsymbol{\kappa},u)=\frac{2}{15\sqrt{\pi}}\int_o^\infty ds\; s\int_{-\pi}^{\pi}d\theta\; e^{-i\boldsymbol{\kappa}\cdot\mathbf{s}}s^{1/2}e^{-s} \times\cos\frac{\theta}{2}\,s\,\exp\left(-\sqrt{8su}/\cos\frac{\theta}{2}\right) \quad (23)$$

where $\kappa_i\equiv k_i s_o$, s/s_o is replaced by s as the integration variable, and $\Lambda(0,0)=1$.

We can obtain an analytic expression for $\Lambda(0,u)$ [set $\boldsymbol{\kappa}=0$ in Eq. (23) and change variables $s\rightarrow\tau/8u$],

$$\Lambda(0,u)=\Gamma(\tfrac{7}{2})^{-1}(8u)^{-7/2}\int_o^\infty d\tau\;\tau^{5/2}e^{-\tau/8u} \times\int_o^{\pi/2}d\theta\;\cos\theta e^{-\sqrt{\tau}\sec\theta}, \quad (24)$$

by evaluating the θ integral

$$I(x)\equiv\int_o^{\pi/2}d\theta\;\cos\theta e^{-x\sec\theta} \quad (25)$$

by considering

$$-\frac{dI(x)}{dx}=\int_o^{\pi/2}d\theta\;e^{-x\sec\theta}=\int_x^\infty dt\;K_0(t) \quad (26)$$

using Sievert's integral (Ref. [23], p. 1000). We integrate Eq. (26) to obtain

$$I(x)=xK_1(x)-x\int_x^\infty dt\;K_0(t). \quad (27)$$

Inserting $x=\sqrt{\tau}$ and $\int_o^\infty dt\;K_0(t)=\pi/2$, Eq. (27) can be written as

$$I(\sqrt{\tau})=\sqrt{\tau}\left(K_1(\sqrt{\tau})+\int_o^\tau dp\;K_0(\sqrt{p})/2\sqrt{p}-\pi/2\right). \quad (28)$$

The τ integral in Eq. (24) is of the form of a $\mathcal{L}$ and using general properties of a $\mathcal{L}$ (Ref. [22] p. 7, No. 41, and p. 79, Nos. 13.2.4 and 13.2.8), we obtain

$$\Lambda(0,u)=\frac{\sqrt{\pi}}{\Gamma(\frac{7}{2})u^{7/2}}\left(u^2\frac{d}{du}\right)^3\{u^{3/2}e^u[K_1(u)+K_0(u)]\} -\sqrt{2\pi}\tfrac{16}{5}u^{1/2}. \quad (29)$$

We use formulas (Ref. [23], p. 376) for the derivatives and recurrence relations for the modified Bessel functions, K, to derive

$$\Lambda(0,u)=p_1e^uK_1(u)+p_2e^uK_0(u)-\sqrt{2\pi}\tfrac{16}{5}u^{1/2}, \quad (30)$$

where p_1 and p_2 are cubic polynomials: $p_1(u)\equiv(u-\frac{52}{15}u^2-\frac{16}{15}u^3)$ and $p_2(u)\equiv(7u+4u^2+\frac{16}{15}u^3)$. In the limit $u\rightarrow 0$,

$$\Lambda(0,u)\simeq 1-\sqrt{2\pi}\tfrac{16}{5}u^{1/2}-7u(\ln u)+O(u). \quad (31)$$

The appearance of $u^{1/2}$ as leading term in the small u behavior of $\Lambda(0,u)$ derives from $\psi(\mathbf{s},t)\sim t^{-3/2}$ for $t\rightarrow\infty$. Equation (31) indicates there is no finite time moment of $\psi(\mathbf{s},t)$, i.e., the density of low velocities in the fracture fragments has a strong influence on the mean time for a transition between fracture intersections. The logarithmic term derives from the specific value of 2 for the power in the exponent in Eq. (16). The accuracy of the expression for $\Lambda(0,u)$ can be determined by the large u limit. Inserting five terms of the asymptotic series for K_1 and K_0 (Ref. [23], p. 378) in Eq. (30), we find

$$\Lambda(0,u)\xrightarrow[u\rightarrow\infty]{}\frac{105\sqrt{\pi}}{(8u)^{7/2}}, \quad (32)$$

which can be checked by an alternate expression for $\Lambda(0,u)$ derived below.

We evaluate the s integral in Eq. (23) for $\boldsymbol{\kappa}\neq 0$; we derive

$$\Lambda(\boldsymbol{\kappa},u)=96\int_{-\pi}^{\pi}d\theta\;\cos\frac{\theta}{2}\,(1+i\boldsymbol{\kappa}\cdot\hat{\mathbf{s}})^{-7/2}e^{z^2}i^6\mathrm{erfc}(z), \quad (33)$$

$$z\equiv\sqrt{2u}\Big/\left(\cos\frac{\theta}{2}\,(1+i\boldsymbol{\kappa}\cdot\hat{\mathbf{s}})^{1/2}\right),$$

where $\hat{s}$ is the unit vector ($\cos\theta$, $\sin\theta$) and $i^n\mathrm{erfc}(z)$ is the nth repeated integral of the complementary error function (Ref. [23], p. 299). If we set $\boldsymbol{\kappa}=0$ in (33) and use the leading term in the asymptotic series (Ref. [23], p. 300),

$$6!\sqrt{\pi}e^{z^2}i^6\mathrm{erfc}(z)\sim 2(2z)^{-7}\sum_{m=0}^{\infty}\frac{(-1)^m(2m+6)!}{m!(2z)^{2m}}, \quad (34)$$

we again obtain Eq. (32). The θ integral in the expression for $\Lambda(\boldsymbol{\kappa},u)$ in Eq. (33) has to be evaluated numerically. In addition to the asymptotic series (34), we will use the analytic properties of $e^{z^2}i^6\mathrm{erfc}(z)$ in the complex u plane and the following representation for the numerical computation:

$$6!\sqrt{\pi}e^{z^2}i^6\mathrm{erfc}(z)=(z^6+\tfrac{15}{2}z^4+\tfrac{45}{4}z^2+\tfrac{15}{8})\sqrt{\pi}e^{z^2}\mathrm{erfc}(z)-z^5 -7z^3-\tfrac{33}{4}z; \quad (35)$$

As outlined in Sec. IV, the determination of the chemical concentration $P(\mathbf{s},t)$ involves both an inverse Fourier transform and an inverse $\mathcal{L}$, Eq. (12). The numerical computation of an inverse $\mathcal{L}$ is notoriously difficult. We derive a very stable form for the numerical evaluation of the inverse $\mathcal{L}$ with analytic continuation in the complex u plane. The function $\Lambda(\boldsymbol{\kappa},u)$ has a branch point at $u=0$, and is analytic in the cut plane, with the branch cut along the negative real u axis. The Fourier transform of $P(\mathbf{s},t)$ is $\gamma(\mathbf{k},t)$, where $\gamma(0,t)=1$ and for $\mathbf{k}\neq\mathbf{0}$,

$$\gamma(\mathbf{k},t)=\int_0^\infty \frac{du\ e^{-ut}}{2\pi i u}\sum_{\pm}(\pm)\frac{1-\Lambda(0,ue^{\pm i\pi})}{1-\Lambda(\mathbf{k},ue^{\pm i\pi})}. \quad (36)$$

We first evaluate

$$\begin{aligned}\Lambda(0,ue^{\pm i\pi})=&p_1(-u)e^{-u}[-K_1(u)\mp i\pi I_1(u)]\\&+p_2(-u)e^{-u}[K_0(u)\mp i\pi I_0(u)]\\&\mp i\sqrt{2\pi}\tfrac{16}{5}u^{1/2},\end{aligned} \quad (37)$$

using the analytic continuation properties of the K Bessel functions (Ref. [23], p. 376), where I_0 and I_1 are the modified I Bessel functions (Ref. [23], p. 374) of order 0 and 1, respectively. For the numerators in the integral in Eq. (36), we can write

$$1-\Lambda(0,ue^{\pm i\pi})=u^{1/2}(\Phi_r\pm i\pi\Phi_i) \quad (38)$$

where

$$\begin{aligned}\Phi_r(u)=&\frac{1-e^{-u}uK_1(u)}{u^{1/2}}-(\tfrac{52}{15}-\tfrac{16}{15}u)u^{3/2}e^{-u}K_1(u)\\&+(7-4u+\tfrac{16}{15}u^2)u^{1/2}e^{-u}K_0(u),\end{aligned} \quad (39)$$

$$\begin{aligned}\Phi_i(u)=&\left(\frac{2}{\pi}\right)^{1/2}\tfrac{16}{5}-(1+\tfrac{52}{15}u-\tfrac{16}{15}u^2)u^{1/2}e^{-u}I_1(u)\\&-(7-4u+\tfrac{16}{15}u^2)u^{1/2}e^{-u}I_0(u).\end{aligned}$$

We can now numerically compute

$$\gamma(\boldsymbol{\kappa},t)=\frac{1}{2\pi i}\int_0^\infty\frac{du}{u^{1/2}}e^{-ut}\sum_{\pm}(\pm)\frac{(\Phi_r\pm i\pi\Phi_i)}{1-\Lambda(\mathbf{k},ue^{\pm i\pi})} \quad (40)$$

by separating the range of integration into the parts $u\leqslant 1$ and $u\geqslant 1$, where the former will dominate for $t\gg 1$. Finally, the inverse $\mathcal{F}$ in Eq. (12) is computed with use of fast Fourier transform (FFT) NAG routines [24]. In Fig. 8, the average (in the y direction) $P(x,t)$ is plotted as a function of s_1 [or $j=-(N-1)/2,\ldots,(N-1)/2$]. The average is computed by setting $k_2=0$ in Eq. (40) and using the one-dimensional $\mathcal{F}^{-1}$ for Eq. (12),

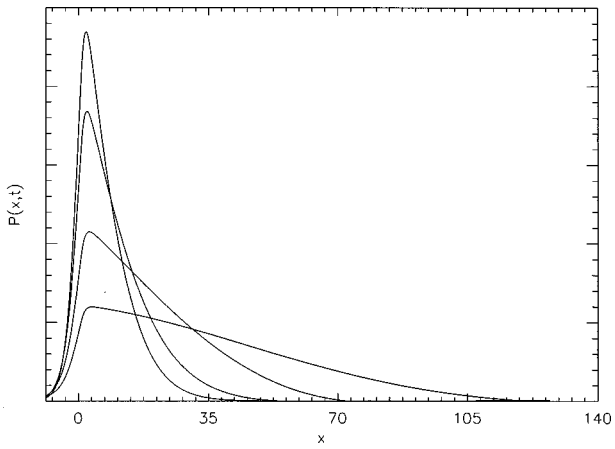

FIG. 8. The vertical average (along the y axis) of $P(\mathbf{s},t)$, defined as $P(x,t)$ (in arbitrary units) vs x (units of length are s_o and time $s_o/2v_o$). Theoretical results are for $t=800$, 2000, 8000, and 30 000; $\beta=\frac{1}{2}$.

$$\begin{aligned}\langle P(j,j_2;t)\rangle_{j_2}=&\frac{e^{-i\pi j}(1-1/N)}{\sqrt{N}}\\&\times\left\{\frac{1}{\sqrt{N}}\sum_{l=0}^{N-1}e^{2\pi ilj/N}e^{[-\pi il(1-1/N)]/N}\right.\\&\left.\times\gamma(\kappa,0;t)\right\},\end{aligned} \quad (41)$$

where $\kappa\equiv 2\pi[l-(N-1)/2]s_0/N$. We evaluate the inverse FFT, in the curly brackets, for values of $N=3^n$, $n=$integer.

A principal result of the CTRW theory is that the progression of the normalized concentration pulse, $P(x,t)$, as shown in Fig. 8, is highly non-Gaussian. The peak of the distribution remains close to the injection point and slowly decreases, while a forward front of particles, with a higher encounter rate of fast transitions, continually advances the concentration profile.

VI. COMPARISON OF CTRW, PARTICLE TRACKING SIMULATIONS AND FIELD DATA

In this Section we make a quantitative comparison of the CTRW theory with the PTS's and with the field data of Fig. 1. We begin by observing that the shapes of the spreading pulse $P(x,t)$ predicted by the CTRW, shown in Fig. 8, are qualitatively the same as those of the $P(x,t)$ found from the PTS's, as shown in Fig. 5, modulo some statistical noise. The theoretical curves in Fig. 8 are limit distributions (as are Gaussians) in that their main features are determined by the small u limit of $\Lambda(0,u)$ in Eq. (31). These features include a peak lying close to the origin, while a tail spreads forward in response to the bias. As time progresses the distribution approaches a ''step function,'' increasingly uniform in space, with the residual position of the ''peak'' indicated by the sharp drop near the origin. This subtlety is reflected in a comparison with the data in Fig. 5. Despite the noise due to the vertical averaging and the relatively small number of realizations, the early time distribution ($t=20$) clearly has a

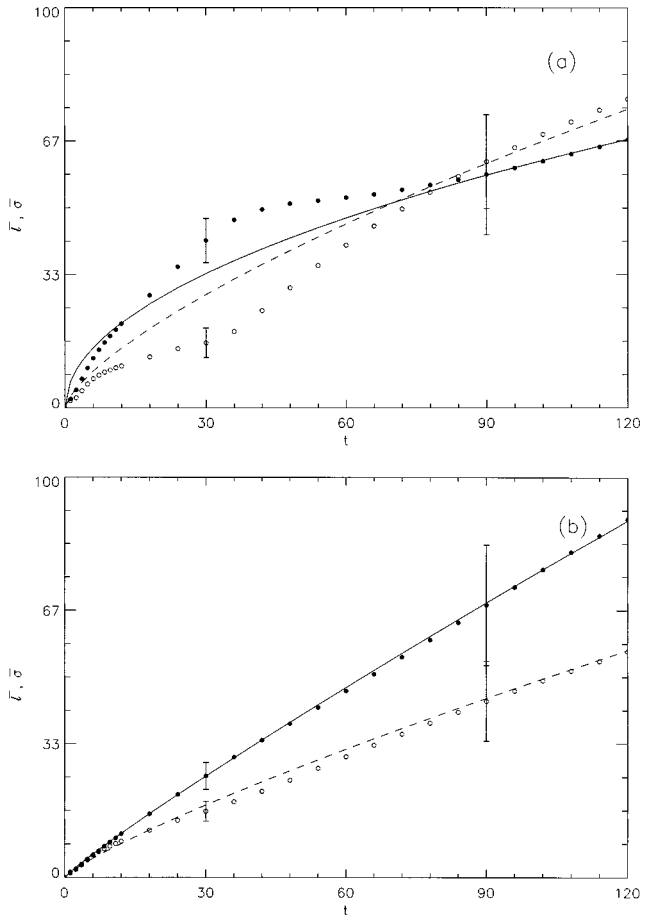

FIG. 9. The mean $\bar{l}(t)$ (●) and standard deviation $\bar{\sigma}(t)$ (○) of $P(x,t)$ vs t (units of length are s_o and time $s_o/2v_o$, where all particle injection points are translated to $x=0$). (a) The average over initial sites of one network generation with the fit of Eqs. (19) and (20) with $\beta\sim 0.5$ (—) and $\beta\sim 0.7$ (---), respectively. (b) The average of 50 realizations with the fit of Eqs. (19) and (20) with $\beta\sim 0.9$ (—) and $\beta\sim 0.8$ (---), respectively. There is an overlap in the error widths of β for $\bar{l}$ and $\bar{\sigma}$.

peak centered in the window $-2<x<14$ with a forward tail extending to $x\lesssim 58$. The later time ($t=50$) has a less defined ''peak'' whose residual position is indicated by the upper part of the drop-off region $x\lesssim 10$, which is close to the estimated peak of the early time curve. The large difference in time scales between Figs. 5 and 8 is due to the difference in β; $\beta=0.5$ in the CTRW case, while, in PTS's, we found that $\beta\sim 0.8$ (cf. below).

A more quantitative analysis of the PTS plume behavior can be achieved, as discussed in Secs. II B and V, by determination of the behavior of $\bar{l}(t)$ and $\bar{\sigma}(t)$ as functions of time. We generated five fracture networks and calculated statistics of the evolving plumes; in each case, we introduced and tracked a large number of particles (5000 were found to be sufficient). For each fracture network generation, $\bar{l}(t)$ and $\bar{\sigma}(t)$ of the PTS's were averaged over a number of initial injection sites. Figure 9(a) shows $\bar{l}(t)$ and $\bar{\sigma}(t)$ for one network generation, together with a fit to Eqs. (19) and (20) for $\beta\sim 0.5$ and $\beta\sim 0.7$, respectively. Although there is some noise in the PTS data, the sublinear t dependence of both $\bar{l}(t)$ and $\bar{\sigma}(t)$ is clear. Moreover, analysis of the PTS behavior in each of the other fracture networks demonstrated the same sublinear t dependence, but with different β values in the range $0.5<\beta<0.9$. An average of these five realizations is shown in Fig. 9(b). Fitting these average results with Eqs. (19) and (20), we find overall exponents of $\beta\lesssim 0.9$ for $\bar{l}(t)$ and $\beta\gtrsim 0.8$ for $\bar{\sigma}(t)$; representative error bars for these averages are also shown. The scant statistics of determining β from $\Phi(\mathbf{v})$ for each generation do not allow us to make an exact comparison with the theory. However, we note that the value $\beta\sim 0.7$, obtained for an averaged $\Phi(\mathbf{v})$ (recall Fig. 7), is well within the error limits of agreement with the β of $\bar{\sigma}(t)$ in Fig. 9(b). Moreover, given the inherent statistical noise in the relatively small fracture networks we examined, it is significant that each separate generation clearly exhibits anomalous transport.

Particle plumes migrating by Gaussian transport can be characterized statistically by the relationships $\bar{l}(t)\sim t$ and $\bar{\sigma}(t)\sim t^{0.5}$, so that $\bar{l}(t)/\bar{\sigma}(t)\sim t^{0.5}$. An extremely important distinguishing feature of anomalous transport is that, in contrast, $\bar{l}(t)/\bar{\sigma}(t)\sim$ const. Referring to our PTS results, and in particular to the fitted (overall) exponents $\beta\lesssim 0.9$ for $\bar{l}(t)$ and $\beta\gtrsim 0.8$ for $\bar{\sigma}(t)$, we stress that the clear deviation of $\bar{l}(t)/\bar{\sigma}(t)$ from the Gaussian dependence of $\sqrt{t}$ is a dominant signature of anomalous transport. This unusual behavior originates in the relatively small, but significant encounter of the particles with a low velocity channel that slows them down for a time much larger than a typical one [18,25]. These smaller numbers of ''slow times'' can be comparable to the accumulation of typical times, and can have a large effect on the distribution of the overall motion of particles. The forward particles can eventually encounter a ''slow'' channel, thus slowing the rate of increase of the mean position, and resulting in a decreasing mean velocity. While it is not obvious, these same dynamics also dominate the standard deviation $\bar{\sigma}(t)$.

Returning now to the field observations of the tracer experiment in a heterogeneous aquifer (see Fig. 1), we observe that the averaged tracer plume shapes are very similar to those of the CTRW and PTS plumes shown in Figs. 5 and 8, respectively. The basic observation is that the peak of the plume persists at the site of injection, and there is a progressive forward advance of tracer. The main point of our analysis is to strongly indicate that the evolution of the entire plume is governed by one mechanism. In Fig. 10, we present a direct comparison of the advance of the measured tracer plume of Ref. [2], Figs. 7(a) and 7(e), and the CTRW theory, using $\beta=\frac{1}{2}$ (cf. below), at two times. The two (nondimensional) times, 500 and 3775 used for the theoretical curves differ by a factor of 7.55, the same as the relative increase in tracer data from 49 to 370 days. These times yielded a good match for the mass distributions. Note that the discrepancies between the peaks in Figs. 10(a) and 10(b) are not significant: the sharp peaks of the tracer data are an artifact of the coarse sampling step sizes. It is important to note that our parameter fit of the theory to these data yields a value of $v_o\approx 5$ m/d; this estimate follows since the dimensionless time equals $2v_o t/s_o$, and as seen from Fig. 10(a), the curve fit was obtained for the dimensionless time of 500 when $t=49$ d, for $s_o\approx 1$ m. This rough velocity estimate is representative of the velocity, giving rise to typical transitions

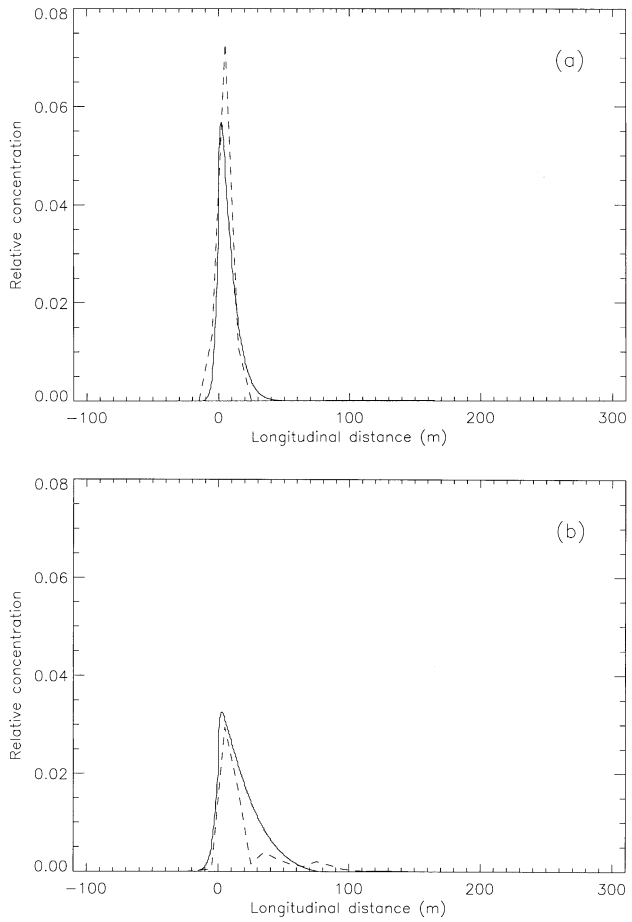

FIG. 10. Comparison of the advance of the measured tracer plume of Ref. [2], Figs. 7(a) and 7(e), and the CTRW theory, using $\beta=\frac{1}{2}$, $s_o\approx 1$ m. (a) Columbus Air Force Base field data (---), $t=49$ days; theory (—), t(nondimensional)$=500$. (b) Columbus Air Force Base field data (---), $t=370$ days; theory (—), t(nondimensional)$=3775$.

(median times), and not the overall mean time of the plume (which is lower, as expected). These estimates are reasonably compatible with the rough velocity estimates suggested in Ref. [2].

Given the considerable degree of uncertainty and noise in the field data (see Refs. [1] and [2] for a detailed discussion of the methods of sampling and data processing, and related uncertainties), the agreement between the field data and the CTRW theory is striking, especially in contrast to the Gaussian distribution comparison used for reference in Fig. 1. It should be stressed that the field data represent one ''realization'' (although averaged in the other two spatial dimensions), while the theory is for an ensemble. If the experiment could have been carried out at different injection sites and then averaged, the fluctuations evident in the forward tail would have been smoother. While there is clearly not an exact one-to-one correspondence between our fracture model—which was used as the basis for the particular formulation of the CTRW model developed here—and the heterogeneous aquifer at the Columbus Air Force Base, there is at least a qualitative correspondence, wherein the preferential flow paths and high flow variability of the heterogeneous aquifer can be mapped to a series of channels or ''fractures.''

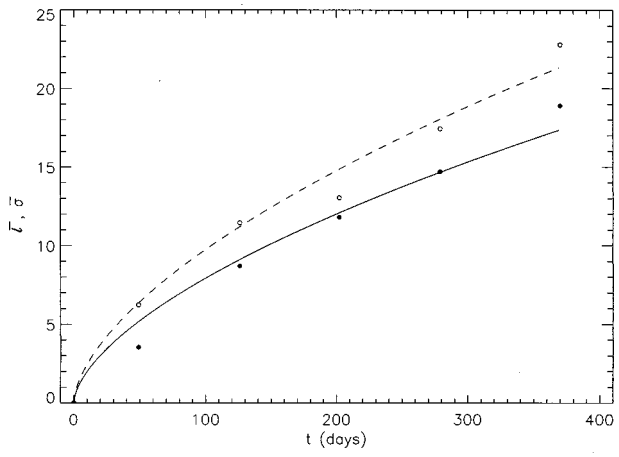

FIG. 11. Behavior of $\bar{l}$ (●) and $\bar{\sigma}$ (○), as functions of time, of the measured tracer plume (points) of Ref. [2], data from Table 1 from the Columbus Air Force Base data. The smooth curves are $\bar{l}\sim t^{0.6}$ (—) and $\bar{\sigma}\sim t^{0.6}$ (---).

The connection between the anomalous transport measured at the Columbus field site and our CTRW framework can be strengthened further. Figure 1 illustrates a clearly anomalous transport behavior. As discussed above, we can analyze the nature of the anomalous transport by considering the behavior of $\bar{l}$ and $\bar{\sigma}$. In Fig. 11, we plot the measured mean displacement $\bar{l}$ and standard deviation $\bar{\sigma}$, along the longitudinal principal axis of the tracer plume, as a function of time. The measured data are from Table 1, snapshots 2–6, of Ref. [2]; we have not included the measured values for snapshot 7 because the radical increase in values indicates either (i) the presence of larger-scale heterogeneities, which are not considered in our current theoretical development; or (ii) a considerable uncertainty in the data, similar to that in the data of snapshot 8 (which were discarded, as discussed in Ref. [2]). Further discussion of this point would require a deeper level of analysis of the data, in which we are now involved.

Significantly, the behavior is clearly non-Gaussian, with exponents for both $\bar{l}$ and $\bar{\sigma}$ of $\sim 0.6\pm 0.1$. This indicates that the mean longitudinal velocity of the plume, defined as $\bar{v}\equiv d\bar{l}(t)/dt$, is decreasing in time (certainly up to 370 days). Moreover, note that the value of $\beta=\frac{1}{2}$ was used in the particular CTRW formulation developed here [see the discussion before Eq. (22)], and in the resulting CTRW solution used for comparison in Fig. 10. We have not tried to optimize our comparison; a value of $\beta=0.6$ would have improved the fit.

VII. SUMMARY AND CONCLUSIONS

We have examined particle transport in a two-dimensional numerical model and in an actual complex geological environment. The numerical model was constructed to emulate basic aspects of a fracture network—intersecting regions of varying lengths, oriented randomly, with different, fixed apertures and simple flow conditions. The most important findings are the nature of the low velocity tail in the velocity distribution,

$$\Phi(\mathbf{v}) \underset{v\to 0}{\sim} v^{1+\beta}, \tag{42}$$

its interplay with the high velocity tail in the same distribution, and the resulting dominant influence on chemical transport patterns. Particle tracking in these fracture networks demonstrated the anomalous, time-dependent behavior of the plume distribution. Mapping the advective flow in each region onto a probability distribution allowed us to use the CTRW to explore the consequences of this low velocity tail on an exponential width $\Phi(\mathbf{v})$; we find that anomalous transport arises for an effective $\beta<1$. The results are less sensitive to all the other details of the system.

We have introduced the CTRW as a good framework to analyze the consequences of Eq. (42); the formalism can effectively use any (normalized) $\psi(\mathbf{s},t)$. The theory has accounted for the non-Gaussian migration of a particle plume. When $\beta<1$, the peak of the distribution remains close to the injection point and slowly decreases (becoming less resolved), while a forward front of particles, with a higher encounter rate of fast transitions, continually advances the concentration profile. The rate of advance of the mean of the plume is proportional to $t^{\beta}(\beta<1)$, slower than the linear proportionality for a plume following Gaussian transport. A significant feature of the CTRW formulation is that once the underlying probability density of particle transitions, $\psi(\mathbf{s},t)$, has been defined [see Eqs. (3) and (18)], the full evolution of a migrating particle plume, including first, second, and higher order moments, and spatial and temporal chemical (particle) breakthrough curves, can be calculated without the need to invoke further assumptions on the transport behavior or characteristics of the flow domain. The actual form of $\psi(\mathbf{s},t)$ can be generalized to deal with a wide variety of flow systems. As more complex flow conditions are incorporated, e.g., into each fracture element (cf. Ref. [26]), the anomalous features of the transport will tend to be emphasized.

Our analysis of field data from experiments carried out at the Columbus Air Force Base is in the spirit of an ''existence proof;'' our intent was to demonstrate the existence of time-dependent anomalous transport in geological formations, and to spur further study of this and other field sites. This system, an averaged three-dimensional, strongly heterogeneous, alluvial aquifer, can be rationalized to share a number of statistical similarities to the simpler two-dimensional numerical fracture model. The model can also be generalized to include an algebraic tail in the distribution of spatial features [an interesting use, in this regard, of the joint $\psi(\mathbf{s},t)$ is in Ref. [27]]. This statistical feature may be present in aquifer systems. The main feature, however, seems to be the same type of low velocity tail in the flow-field distribution. Thus one important question that arises is: What are the properties of a random system which result in Eq. (42)? The answer to this question, and analysis of anomalous transport using the CTRW framework in other actual field systems, remain the subject of future studies.

ACKNOWLEDGMENTS

The authors thank Tom Clemo for sharing his computer code, Eli Galanti for assistance, and Martin Blunt for useful discussion. B.B. thanks the European Commission, Environment and Climate Programme for partial support. H.S. thanks the Sussman Family Center for Environmental Sciences for partial support.

[1] J. M. Boggs, S. C. Young, L. M. Beard, L. W. Gelhar, K. R. Rehfledt, and E. E. Adams, Water Resour. Res. **28**, 3281 (1992).
[2] E. E. Adams and L. W. Gelhar, Water Resour. Res. **28**, 3293 (1992).
[3] J. C. S. Long and K. Karasaki, Swedish Nuclear Fuel and Waste Management Co., Stockholm, Technical Report No. 92-06, 1992.
[4] N. A. Chapman and I. A. McKinley, *The Geological Disposal of Nuclear Waste* (Wiley, Chichester, 1987).
[5] B. Berkowitz, in *Advances in Porous Media*, edited by Y. Corapeioglu (Elsevier, Amsterdam, 1994), Vol. 2, p. 397.
[6] G. Dagan, *Flow and Transport in Porous Formations* (Springer-Verlag, Berlin, 1989).
[7] J. H. Cushman and T. R. Ginn, Transp. Porous Media **13**, 123 (1993).
[8] L. W. Gelhar, *Stochastic Subsurface Hydrology* (Prentice-Hall, Englewood Cliffs, NJ, 1993).
[9] J. Glimm, W. B. Lindquist, F. Pereira, and Q. Zhang, Transp. Porous Media **13**, 97 (1993).
[10] S. P. Neuman, Water Resour. Res. **29**, 633 (1993).
[11] M. Sahimi and A. O. Imdakm, J. Phys. A **21**, 3833 (1988).
[12] B. Berkowitz and H. Scher, Phys. Rev. Lett. **79**, 4038 (1997).
[13] H. Scher and M. Lax, Phys. Rev. B **7**, 4491 (1973).
[14] T. Clemo, Ph.D. thesis, University of British Columbia, Vancouver, 1994.
[15] J. C. S. Long, J. S. Remer, C. R. Wilson, and P. A. Witherspoon, Water Resour. Res. **18**, 645 (1982).
[16] F. W. Schwartz and L. Smith, Water Resour. Res. **24**, 1360 (1988).
[17] B. Berkowitz, C. Naumann, and L. Smith, Water Resour. Res. **30**, 1765 (1994).
[18] H. Scher, M. F. Shlesinger, and J. T. Bendler, Phys. Today **44** (1), 26 (1991).
[19] S. Imamura, T. Kitamura, and N. Nakamura, Jpn. J. Appl. Phys., Part 2 **23**, L537 (1984).
[20] H. Scher and E. W. Montroll, Phys. Rev. B **12**, 2455 (1975).
[21] M. F. Shlesinger, J. Stat. Phys. **10**, 421 (1974).
[22] G. E. Roberts and H. Kaufman, *Table of Laplace Transforms* (Saunders, Philadelphia, 1966).
[23] *Handbook of Mathematical Functions*, edited by M. Abramowitz and I. A. Stegun (Dover, New York, 1965).
[24] NAG—The Numerical Algorithms Group, Ltd. (Oxford, United Kingdom, 1985).
[25] B. Berkowitz and H. Scher, Water Resour. Res. **31**, 1461 (1995).
[26] Y. W. Tsang and C. F. Tsang, Water Resour. Res. **25**, 2076 (1989).
[27] J. Klafter, A. Blumen, and M. F. Shlesinger, Phys. Rev. A **35**, 3081 (1987).